45th AIAA Aerospace Sciences Meeting and Exhibit
8 - 11 January 2007, Reno, Nevada

AIAA 2007-1115

Grid Sensitivity of Detached eddy simulation of a Mach 16 Re-entry Configuration

Krishnendu Sinha*
Indian Institute of Technology Bombay, India 400076
and
Graham V. Candler†
University of Minnesota, Minneapolis MN 55455

Abstract

This paper presents analysis of hypersonic base flows using the detached eddy simulation (DES) methodology. Unlike Reynolds-averaged Navier-Stokes (RANS) simulations, DES computes the dominant unsteady motion in the three-dimensional flow behind a vehicle, and thus results in a more realistic flow field than RANS. Simulations are performed on carefully designed DES grids and the effect of grid refinement in the focus region is studied. At the current conditions the flow in the near wake is transitional. Successive grid refinement in this case reduces the magnitude of the eddy viscosity such that the DES solution on the finest mesh approaches direct simulation without a turbulence model. In the absence of significant eddy viscosity, lowering of numerical dissipation is essential to achieve grid-converged solution.

Introduction

Aerodynamic and thermal loads on the afterbody of re-entry vehicles are important in vehicle drag, heat shield design, payload placement and stability. There is considerable uncertainty in predicting the afterbody and wake flow field, which is often compensated by large factor of safety in the heat shield design.[1] The Reynolds number in the later part of re-entry can be high enough for transition to turbulence in the wake. Turbulent mixing alters the structure of the wake and significantly increases the heat transfer rate to the afterbody. Therefore, validation of current and advanced simulation methods for turbulent separated flows under these high Mach number conditions is important.

Wright *et al.*[1] present a concise review of computational research on aero-thermal characterization of afterbody flow fields. The majority of the previous work focuses on laminar conditions that typically prevail at high altitudes. Only a limited number of studies address transitional or turbulent flows. Brown[2] compares several turbulence models against heat transfer data on the afterbody of a configuration similar to the Mars Pathfinder spacecraft. Nance *et al.*[3] use a transition prediction method along with an existing turbulence model to study a similar configuration. In both cases, however, the presence of a sting contaminates the free-flight wake closure and therefore the assessment of heat transfer rate.

Until recently, engineering prediction of turbulent flows relied exclusively on Reynolds-averaged Navier Stokes (RANS) simulations that compute the time-averaged flow field. However, RANS turbulence models can yield significant error in regions of large-scale separation. Detached eddy simulation (DES)[4] improves predictions in massively separated flows by simulating the unsteady dynamics of the dominant length scales away from solid walls and applying RANS only in the near wall region. DES has mostly been used in low-speed flows, with limited application at supersonic speed. In supersonic base flows, DES is found to accurately predict the extent of the recirculation region and the base pressure.[5]

Detached eddy simulation was used for the first time to investigate the afterbody flow field of re-entry vehicles in Ref. 6 . These are typically blunt body configurations with a large well-defined recirculation region at the base, which makes them an ideal test case for the application of DES. These high Mach number flows are marked by strong shocks in front of the body and large flow expansion around the shoulder, which need to be captured accurately to get the correct upstream conditions for the base flow. This makes the simulation of hypersonic flows much more challenging than their supersonic counterparts. A multi-block grid topology was used in Ref. 6 to

---

* Assistant Professor, Department of Aerospace Engineering, Indian Institute of Technology Bombay. Member AIAA.
† Professor, Aerospace Engineering and Mechanics, University of Minnesota, Associate Fellow AIAA.

capture the different aspects of the flow field. The simulations predicted a complex three-dimensional unsteady flow in the recirculation bubble behind the vehicle. The resultant afterbody heating rate and pressure, both instantaneous and time-averaged values, are discussed. Compared to a three-dimensional laminar solution, DES was found to predict a higher heating rate and lower pressure on the afterbody.

The results in Ref. 6 , although interesting, are probably limited by the accuracy of the time integration method, poor grid quality in certain locations and, most important, lack of a grid-refinement study. The time-averaged results also indicate the need for longer temporal averaging of the solution. In this follow-up work, the same re-entry configuration is re-investigated using a second-order accurate time-integration method and computational grids that are carefully designed to meet the DES criteria. The effect of grid refinement on the results is also presented, which bring out a potential limitation of the DES methodology in high Mach number applications.

The typical Reynolds number encountered in manned-capsule atmospheric re-entry configurations are much lower than those in low-speed applications, and often the conditions of practical interest are at most transitional. Evaluating the performance and limitations of the DES methodology in these low Re conditions is the main objective of this paper. This work also aims to study the heat transfer prediction by RANS/LES hybrid methodology like DES. Unlike pressure data, heating rate predictions are expected to be sensitive to the RANS model effective close to the vehicle surface, as well as to the RANS/LES transition location. This may limit the potential of DES in hypersonic re-entry configurations. As in Ref. 6, the effect of thermo-chemistry is not considered in the current simulations because it increases the computational requirements significantly. Even the current perfect gas simulations stretch the limits of existing computational resources. Compressibility effects, which may be significant at these high Mach numbers, are also not included. These aspects, although necessary for a fully validated quantitative prediction, are not essential to answer the specific questions addressed in the current study.

The remainder of the paper is organized as follows. The vehicle geometry and test conditions are given in the next section. This is followed by a description of the solution methodology and design of computational grids. The instantaneous and time-averaged results obtained using DES are then presented. Finally, the effect of grid refinement in the re-circulation region on the time-averaged solution is discussed.

Vehicle geometry and flow conditions

The vehicle geometry used in the current work, shown in Fig. 1, corresponds to the Fire II re-entry configuration in the later part of its trajectory after the first two heat-shields are jettisoned. The freestream conditions correspond to the 35 km altitute condition.[7] The density, temperature and velocity at this trajectory point are 0.0082 kg/m^3, 237 K and 5 km/s (Mach 16), respectively. The surface temperature is taken to be 553.3 K based on the in-flight calorimeter measurements.[7] The angle of attack is assumed to be zero, because the angle-of-attack variations in flight had very little effect on the measured afterbody data. The Reynolds number based on free stream conditions and body diameter is 1.76×10^6. Blunt body separation shear layer and inner wake transition correlations are presented by Lees,[8] where the transition Reynolds number is given as a function of the local Mach number outside the wake. Based on these correlations and data from preliminary simulations, the wake is expected to transition upstream of the neck.

Simulation Methodology

The flow field around the re-entry configuration is simulated by solving the three-dimensional Favre-averaged Navier-Stokes equations. The numerical method uses a modified (low dissipation) form of Steger-Warming flux vector splitting[9] for evaluating the convective fluxes. Central differencing is used for the viscous fluxes and source terms. The turbulence model equation is fully coupled with the mean flow equations and the code is implemented in parallel using the Message Passing Interface.[10] The code has been systematically validated for flat plate boundary layers and blunt body flows. An axi-symmetric version of the code has also been applied to shock-shock interaction flows.[11]

Detached eddy simulation based on the Spalart-Allmaras (SA) turbulence model[12] solves the following conservation equation for variable $\tilde{\nu}$ which is related to the eddy viscosity ν_t.

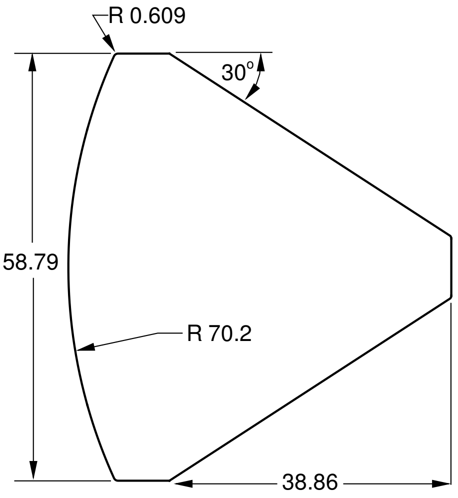

Figure 1. Fire II re-entry configuration used in the current simulations. All dimensions are in cm.

$$\frac{D\bar{\rho}\tilde{\nu}}{Dt} = c_{b1}\bar{\rho}\tilde{S}\tilde{\nu} - c_{w1} f_w \bar{\rho}\left[\frac{\tilde{\nu}}{d}\right]^2 + \frac{\bar{\rho}}{\sigma}[\nabla\cdot((\nu+\tilde{\nu})\nabla\tilde{\nu}) + c_{b2}(\nabla\tilde{\nu})^2]$$

The left hand side represents the material derivative of $\bar{\rho}\tilde{\nu}$, and the terms on the right hand side correspond to production, destruction and diffusion mechanisms in the flow. The turbulent viscosity is given by

$$\nu_t = \tilde{\nu} f_{v1}\,, \quad f_{v1} = \frac{\chi^3}{\chi^3 + c_{v1}^3}\,, \quad \chi = \frac{\tilde{\nu}}{\nu}\,.$$

S is the magnitude of the mean vorticity and

$$\tilde{S} = S + \frac{\tilde{\nu}}{\kappa^2 d^2} f_{v2}\,, \quad f_{v2} = 1 - \frac{\chi}{1 + \chi f_{v1}}\,,$$

The wall destruction function is

$$f_w = g\left[\frac{1 + c_{w3}^6}{g^6 + c_{w3}^6}\right]$$

and

$$g = r + c_{w2}(r^6 - r)\,, \quad r = \frac{\tilde{\nu}}{\tilde{S}\kappa^2 d^2}$$

The constants in the equation are:

$$c_{b1} = 0.1355\,, \quad \sigma = \frac{2}{3}\,, \quad c_{b2} = 0.622\,,$$

$$\kappa = 0.41\,, \quad c_{w1} = \frac{c_{b1}}{\kappa^2} + \frac{1 + c_{b2}}{\sigma}\,, \quad c_{w2} = 0.3\,,$$
$$c_{w3} = 2\,, \quad c_{v1} = 7.1\,.$$

The defining length scale of the SA model is the distance to the closest wall d. To make the model operate in DES mode one simply substitutes a new length scale d_{des} in place of d. d_{des} is defined as:

$$d_{des} = \min(d, C_{des}\Delta)$$

where Δ is the largest dimension of the local grid cell. In the near-wall region, $d_{des} = d$ and the model works in the RANS mode. Away from solid walls, $C_{des}\Delta < d$ and the destruction term is balanced by production. This results in $\nu_t \propto S\Delta^2$ which is similar to the Smagorinski model for sub-grid scales in a large eddy simulation

(LES). Thus, the method switches to LES mode away from solid walls. Here, C_{des} is an adjustable parameter which was calibrated by Shur *et al.*[4] in simulations of isotropic turbulence and is set to 0.65. We use the same value of the constant in our calculations.

The numerical method is second-order accurate in space and time. Similar numerics have been used in detached eddy simulation of supersonic base flows.[5] An implicit full matrix Data-Parallel Lower-Upper Relaxation method[13] is used to integrate the equations in time. The method involves Newton sub-iterations to converge the L_1 norm of the density residual to a prescribed tolerance, taken to be 10^{-6} of a characteristic density in the flow. First order backward Euler time integration is also implemented in the code and is mainly used to integrate through the initial transient flow development.

Grid Design

DES works in the RANS mode in the attached regions of the flow. This includes the forebody and shoulder of the vehicle. Two-dimensional axi-symmetric RANS solutions of the current configuration using the Spalart-Allmaras model are presented in Ref. 14. The salient features of the two-dimensional grids are listed below, and they were used to guide the development of the current three-dimensional volume grids. The outer boundary is carefully tailored such that the grid lines on the forebody are closely aligned with the bow shock wave. A wall-parallel spacing of 1.4×10^{-5}m is required in the nose stagnation region to obtain a grid-independent solution. Along the forebody and shoulder, a wall normal spacing of 1×10^{-5} m is needed to accurately predict the vehicle heating rates, whereas a much coarser grid (5×10^{-5} m) is sufficient on the afterbody.

The baseline volume grid generated for detached eddy simulation is shown in Fig. 2. The multi-block grid has one-to-one grid point matching at the inter-block boundaries. The forebody is spanned by grid blocks I and III. The axi-symmetric grid block III is generated by a revolution of the two-dimensional RANS grid about the vehicle axis. Thus, wall-normal and wall-parallel grid resolution on the forebody and shoulder is maintained to be the same as in Ref. 14. The azimuthal spacing is dictated by the afterbody grid, as discussed below. In order to avoid grid singularity at the vehicle axis, a non-axisymmetric grid block I is used at the nose. This significantly reduces the grid-sensitivity of the solution in the nose stagnation region. Wall-parallel grid spacing much larger than that in the axi-symmetric simulation could be used. The distribution of points in the wall-normal direction is identical to the RANS grid. On the afterbody, grid blocks II and IV are constructed to allow a careful resolution of the wake, and the region outside the wake is spanned by grid block V. The flow in the outer inviscid region is expected to be relatively steady, axi-symmetric, and similar to the RANS solution. The grid spacing in block V is therefore maintained to be smaller than or comparable to that used in the axi-symmetric simulation

The objective of a detached eddy simulation is to resolve the dominant unsteady scales in the wake flow. This zone is divided into the focus and departure regions as shown in Fig. 2d. The focus region of a detached eddy simulation is defined by "can a particle return from this point to very near the body?"[15] For the current configuration, it corresponds to the conical separation bubble behind the vehicle that extends from the separation location at the shoulder to the neck (at about $1D$ downstream of the base). The focus region is identified based on preliminary simulations. The large-scale unsteady motion in the focus region should be well resolved, and the grid is therefore carefully designed to achieve cell sizes smaller by two orders of magnitude than the overall size of the recirculation region.[15] A target grid spacing Δ_0 of 0.025 D is used in the baseline simulation. The wall-parallel grid spacing near the separation location and in the vicinity of the expansion corner at the base are much smaller than Δ_0. In the near wall region, DES reverts to the RANS model and therefore the wall-normal spacing of 5×10^{-5}m is maintained based on the axi-symmetric RANS results.[14]

Spalart[15] advocates the use of isotropic cells in the focus region. This enables one to obtain the desired Δ_0 with the minimum number of grid points. Finer spacing in one or two directions is generally wasted. The grid topology in block II (see Fig. 2c) with relatively uniform spacing in a cross-sectional plane is especially suited to obtain isotropic cells. The axial grid spacing in this block is tailored to maintain the cell aspect ratio close to unity until the end of the focus region. In the axi-symmetric block IV, the grid in an azimuthal plane is designed to have cell aspect ratios close to unity, and the points are uniformly distributed in the circumferential direction. The number of azimuthal points is determined by the grid spacing requirement of Δ_0 which is most stringent near the shoulder. The axi-symmetric topology in this grid block precludes constant circumferential spacing along the length of the conical frustum. The largest spacing is near the shoulder, which along with fine spacing in the wall-parallel and wall-normal directions result in highly anisotropic cells around this location. The implications of these high aspect ratio cells on the flow solution will be discussed in the next section.

The departure region extends from the neck to the exit boundary at $5D$ downstream of the base. This region is confined to grid block II, and the grid in the axial direction is stretched exponentially to the exit boundary. In the radial direction, a relatively fine grid is maintained to capture the flow gradients across the wake. The overall three-dimensional multi-block grid consists of 2.6×10^6 points out of which 9.4×10^5 grid points are concentrated in the focus region.

The wake flow simulations are known to be extremely sensitive to volume grid generation especially near separation at the shoulder.[1] A careful grid refinement study was undertaken in Ref. 14 to ascertain grid independence of the RANS solution near the separation point. In this region DES works in the RANS mode, and therefore the current three-dimensional grids with comparable spacing at the shoulder are expected to be sufficient for solution accuracy.

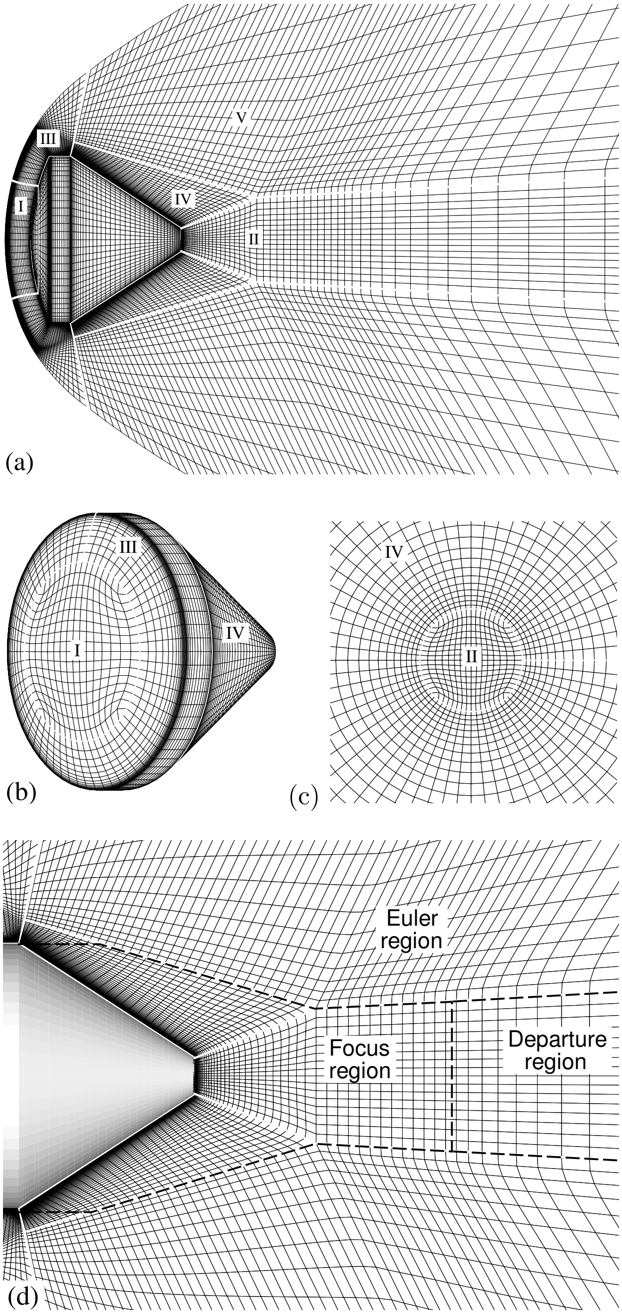

Figure 2. Three-dimensional grid for detached eddy simulation: (a) multi-block topology, (b) grid layout on the vehicle, (c) grid layout on the base, and (d) magnified view of the wake grid. Every second point in each direction is shown. White lines denote grid block boundaries, and dashed lines demarcate DES flow regions.

Simulation Results

The solution is initialized to free-stream quantities everywhere except in the vicinity of the base where the velocity is set to zero. To quickly set up a realistic flow pattern around the vehicle, the solution is computed using the relatively inexpensive first-order backward Euler time-integration method up to 82 t_{flow}. The characteristic flow time t_{flow} is defined in terms of the vehicle diameter and freestream velocity. Second-order time integration is then used to obtain time-accurate results, and the simulation is run for 48 t_{flow} to get past any transient development. Time is set to zero at this point and mean flow statistics are gathered thereafter. Allowing for a longer transient time is found not to alter the time-averaged results.

The time step used in the current simulation is 0.012 t_{flow}. This is equivalent to a CFL number (based on local cell size and the magnitude of the largest wave propagation speed) of 106. A second computation of the same flow field used a smaller time step of 0.0012 t_{flow}. Pressure time histories at two representative points in the near wake are plotted in Fig. 3. The results obtained using Δt of 0.012 t_{flow} (lines) were found to be identical to those computed with the smaller time step (symbols). Thus the larger Δt is adequate to accurately reproduce the temporal evolution of the unsteady wake. At $\Delta t = 0.0012\ t_{flow}$, 3-4 sub-iterations were required to converge the solution at each time step. Using Δt of 0.012 t_{flow} required about 18 sub-iterations per time step, thereby reducing the overall computing time by more than 40% as compared to the smaller Δt. Using Δt larger than 0.012 t_{flow} resulted in a steep increase in the number of sub-iterations per time step, and was therefore found to be inefficient. Note that the smallest time-scale of unsteadiness was found to be about 0.3 t_{flow} in the current simulation.

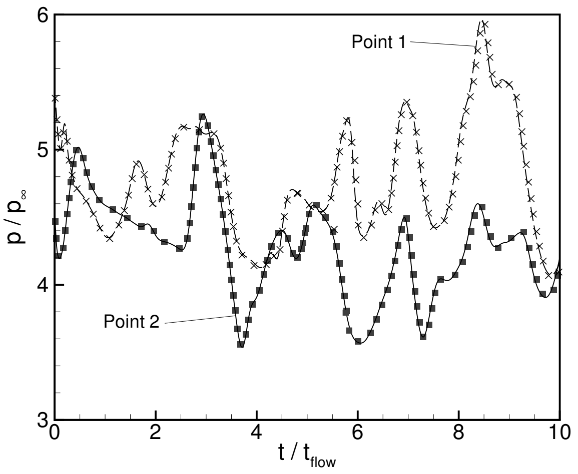

Figure 3. Pressure time histories at two representative points in the recirculation region computed using $\Delta t = 0.012\ t_{flow}$ (lines) and 0.0012 t_{flow} (symbols).

The instantaneous temperature contours in Fig. 4a identifies the salient features of the flow field. These include the bow shock, expansion at the shoulder, a large recirculation region, and the recompression shock generated at the neck. Note that the wake flow is mostly subsonic upstream of the neck. The flow in the recirculation region is highly unsteady and three-dimensional with a range of length and time scales. This leads to unsteady pressure and heating rates on the afterbody. The localized peak heating can be appreciably higher than the time-averaged values. The flow outside the wake is mostly steady and axisymmetric, with minimal effect of the wake unsteadiness. The time-averaged temperature distribution is shown in Fig. 4b. The main difference from the instantaneous flow is in the recirculation bubble which is dominated by a single toroidal votex in the time-averaged flowfield. The temperature contours are close to being axisymmetric. A more detailed description of the flow field can be found in Ref. 16.

The time-averaged pressure and heat transfer rate on the forebody are presented in Fig. 5 (shown by symbols). Here, s is the local arc-length measured from the nose of the vehicle. The normalized pressure shows a parabolic profile on the forebody with a rapid decrease as the flow expands around the shoulder. The heating rate is relatively constant on the forebody with localized peaks at the expansion corners. The flow expansion and cooling results in a much lower heat flux on the shoulder. Data from the axi-symmetric RANS simulations in

Ref. 14 (shown by lines in Fig. 5) are found to match the current results, except for a small discrepancy (about 1%) in the nose stagnation point heating rate.

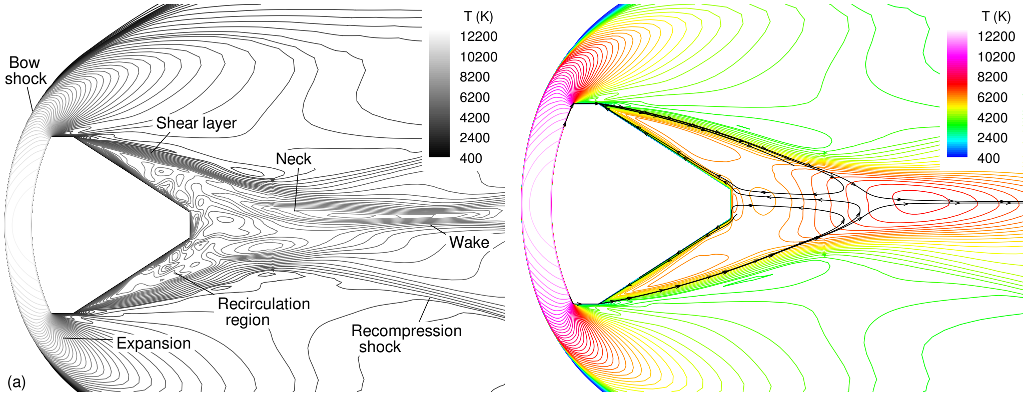

Figure 4. Temperature contours in a plane through the vehicle axis: (a) single time-realization at 264 t_{flow}, and (b) time-averaged distribution over 300 t_{flow}. A few representative streamlines are shown to identify the flow pattern.

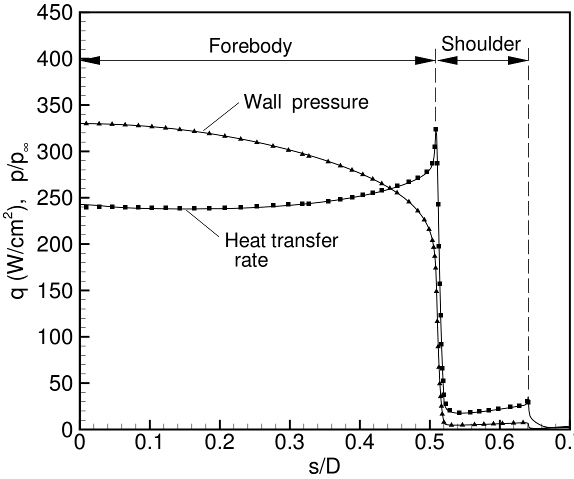

Figure 5. Normalized pressure and heat transfer rate on the forebody and shoulder of the vehicle. Results obtained from the current simulation (symbols) are compared to RANS predictions (line) from Ref. 14.

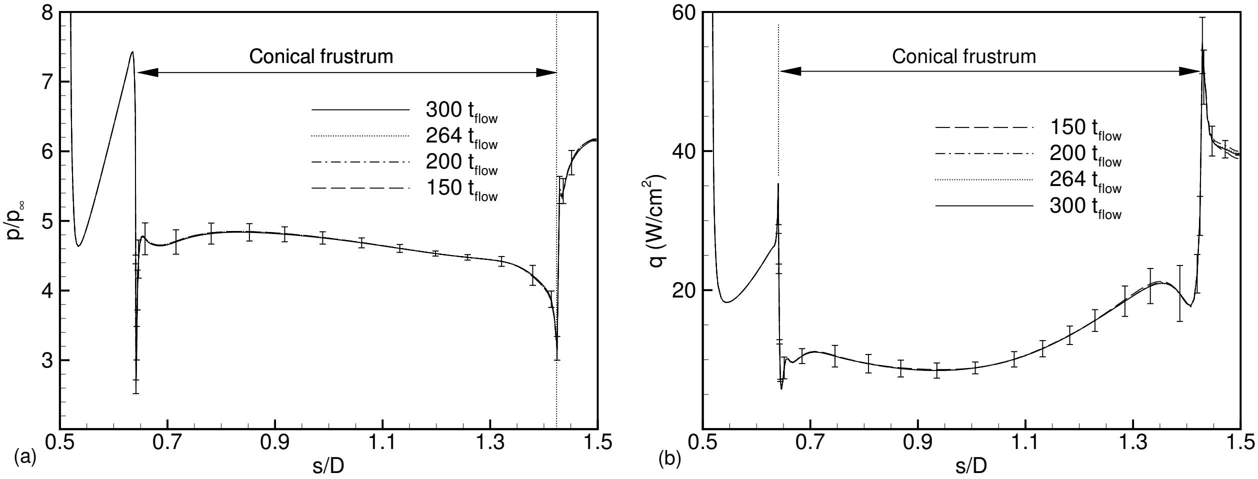

Figure 6. Time-averaged normalized wall pressure and heat transfer rate on the vehicle afterbody obtained using different averaging time intervals. The lines correspond to the circumferential mean at a given axial location, and the error bars represent the circumferential variation in the data for 300 t_{flow} case.

Figure 6 shows the time-averaged normalized pressure and heat transfer rate on the afterbody. The pressure on the conical frustum is relatively constant and is about 1.5% of the nose stagnation pressure. The pressure on the flat base is somewhat higher because of the reverse flow stagnating in this region. The heat transfer rate on the conical frustum varies between 4 and 8% of the nose stagnation point heating rate. The larger values are found close to the base. The expansion corner at the two ends of the conical frustum are characterized by high local heat flux, and the stagnating flow on the base results in as high as 16% of the nose stagnation point heat flux. As pointed out earlier, the time-averaged afterbody flowfield is not entirely axi-symmetric. The lines in Fig. 6 correspond to the circumferential mean of the time-averaged data at a given axial location, and the circumferential variation is shown by the error bars. The maximum circumferential variation in the time-averaged wall pressure is about ± 7 % of its mean value. A majority of the variation is found in the vicinity of the separation point at the shoulder and near the base. The highest circumferential variation in the heat flux (± 21 %) is found near the base-frustum corner.

Figure 6 also shows the effect of the averaging time-interval on the results. The mean wall pressure obtained using data over 150, 200, 264, and 300 t_{flow} are identical, but the circumferential variation shows a gradual decrease with increasing averaging time-interval. The different integration times have a negligible effect on the afterbody heat transfer rate except for the base region. There is a noticeable difference between the results obtained using 150, 200, and 264 t_{flow}, but the last two cases (264 and 300 t_{flow}) are identical. This implies that time-averaging over an interval of about 250 t_{flow} is sufficient to obtain converged heat transfer data.

Grid refinement study

The effect of grid spacing in the focus region is assessed by computing the solution on two additional grids. The fine grid is obtained by refining the focus region baseline grid spacing by a factor of two in each direction and the grid spacing is increased by about 32% in the coarser grid. The requirement of a minimum of 32 points in each direction ($D/\Delta_0 \sim 32$) precludes increasing Δ_0 further. Similar to the baseline grid, the wall-normal spacing in the RANS region next to the wall is maintained at 5×10^{-5} m based on axi-symmetric RANS results.[14] The total number of grid points in each case along with the number of points in the focus region are listed in Table I.

Three-dimensional unsteady solutions were computed on the two additional grids and the time-averaged results are presented below. The characteristics of the three simulations are also included in Table I. The number of processors used in each case was determined by the need for load balancing among processors and to obtain time-averaged data with in a reasonable amount of time. The time-step was decreased for the fine grid simulation and was increased for the coarser grid. These time-step values are within the range that was tested for accuracy in the baseline simulation. A larger time-step in the coarse grid case required larger number of sub-iterations per time-step compared to the other simulations. The CPU time per t_{flow} in the fine grid is comparable to the baseline case because of the increased number of processors employed for the larger grid. The coarse grid simulation is considerably faster.

Grid	Coarse	Baseline	Fine
Focus region target grid size (Δ_0/D)	0.033	0.025	0.0125
Total grid points ($\times10^6$)	1.42	2.57	9.20
Points in focus region ($\times10^6$)	0.45	0.94	4.20
Number of processors	26	22	44
Maximum points per processor($\times10^3$)	57.6	120	233
Time step (t_{flow})	0.023	0.012	0.006
No. of sub-iterations per time-step	27-30	18-20	5-7
CPU time per t_{flow} (hour)	0.69	1.67	1.90
Integration time (t_{flow})	250	300	300
Overall computational time (cpu-hour)	5564	13222	30096

Table I. Characteristics of the three computational grids and the respective simulations. CPU time is based on 2.4 GHz Xeon microprocessors.

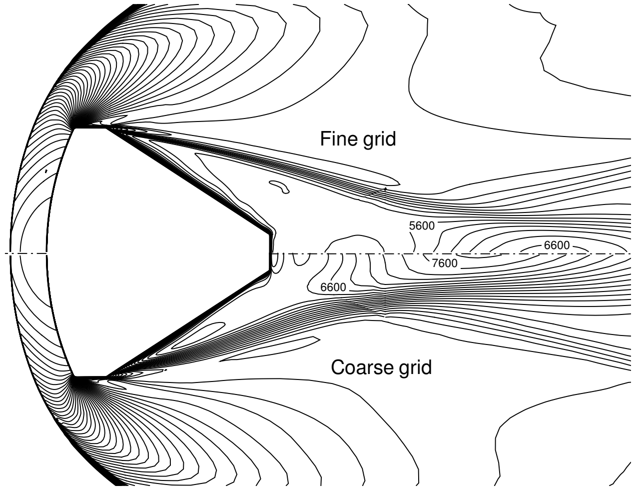

Figure 7. Time-averaged temperature field computed using the fine grid (top half) and coarse grid (bottom half).

The mean temperature field plotted in Fig. 7 shows lower temperature in the wake region for the finer grid (top half) than for the coarser mesh (bottom half). The baseline solution (see Fig. 4b) is in between the other two, though it is closer to the coarse grid solution. This trend is mainly due to the decreasing eddy viscosity with grid refinement that results in lower turbulent dissipation of kinetic energy into internal energy. A closer inspection also reveals that the size of the separation bubble and the distance of the neck from the vehicle base increase with grid refinement. The peak temperature at the neck is located at $x/D = 1.74$, 1.84, and 2.04 for the three grids in the order of refinement. As expected the flowfield outside the wake, including that on the forebody and shoulder, is not affected by refining the focus region grid.

The size of the separation region computed on the three grids correlates directly to the afterbody pressure in each case (see Fig. 8a). A smaller wake in the coarse grid simulation results in a lower pressure on the afterbody as compared to the larger wake in the fine grid solution. In addition, the finer grid simulation resolves smaller structures in the wake that lead to better mixing, and thereby a more uniform pressure on the afterbody frustum. The base pressure is also found to be comparable to the frustum value in the fine grid solution, unlike the other two cases. Note that a grid independent solution is not obtained in this flow in spite of using a large number of grid points. The reason for this behavior is explained below.

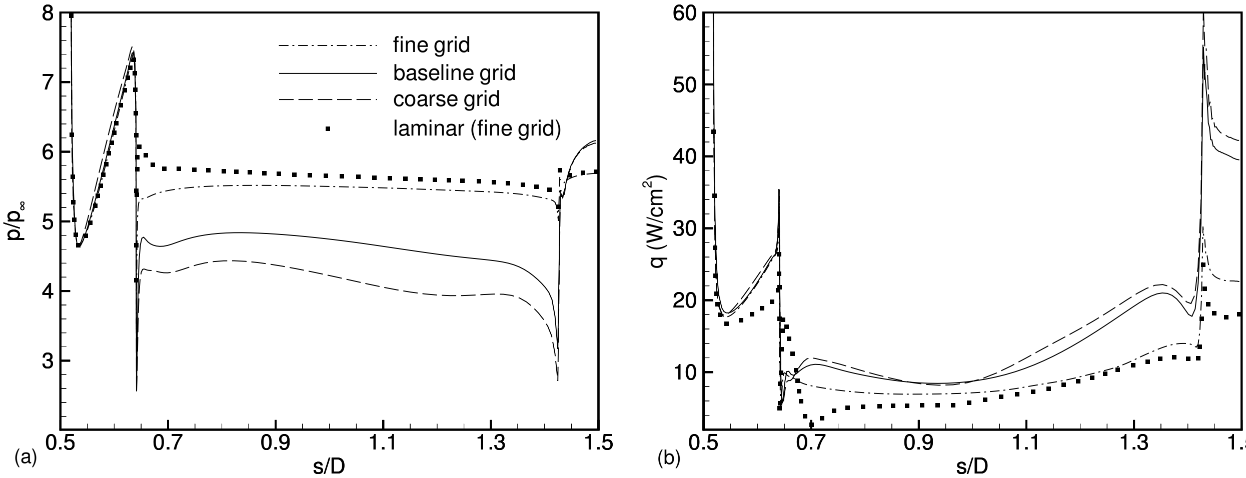

Figure 8. Effect of grid refinement on the time-averaged pressure and heat transfer rate on the Fire II afterbody.

As the focus region grid is refined, the magnitude of the eddy viscosity decreases ($\nu_t \propto \Delta^2$). This is because a larger range of length scales is resolved on a finer grid and a smaller fraction of the turbulent kinetic energy is modeled by the eddy viscosity. The overall contribution of Reynolds stresses to the mean flow is however maintained. This leads to grid independence of the time-averaged solution as long as the magnitude of the eddy viscosity is significantly larger than the molecular viscosity and numerical dissipation in the simulation. This is common at high Re conditions and grid-converged solution in such flows has been achieved using detached eddy simulation.[5]

By comparison, at transitional Re typical of the current simulations, successive grid refinement can lead to a situation where the eddy viscosity is no longer dominant (e.g. $\nu_t/\nu \sim 1$ in the focus region of the fine grid simulation). Thus the turbulence model has minimal effect on the solution, as can be seen from the fact that the DES wall pressure on the fine grid is close to the laminar results obtained on the same grid. The size of the recirculation regions are also similar. The only difference is in the vicinity of the separation point where the time-averaged laminar data show a small secondary separation bubble. Thus the DES computation on the fine grid approaches direct calculation, without a turbulence model, of the three-dimensional unsteady flow in the wake. In such a case, detached eddy simulation fails to achieve a grid-independent solution via the compensating effects of resolved and modeled parts of the Reynolds stresses.

In the absence of significant turbulent eddy viscosity, control of the numerical dissipation becomes the key to obtaining grid-converged results. This can be achieved by using higher-order numerical methods with low dissipation characteristics. In the limit of vanishing numerical dissipation, a detached eddy simulation with insignificant eddy viscosity will become a direct simulation where all relevant length and time scales of turbulence are computed. Direct numerical simulation of the wake flow is beyond the scope of the current paper. Thus, successive grid refinement does not lead to a grid-independent time-averaged solution in the current flow. The inherent limitation of DES at low Re therefore precludes establishing the spatial convergence accuracy of the solution. However, the temporal and iterative convergence accuracy of the results obtained on each grid is demonstrated in this work.

The heat transfer results in Fig. 8b show an interesting trend. The heating rates obtained using the baseline and coarser grids are comparable, while the fine grid results in 40-50% lower heat flux on the frustum and base. Note that the fine grid DES data are close to the laminar results except in the vicinity of the separation point. The variation of heating rate between the coarse, baseline and fine grid DES can be explained in terms of the temperature profile across the boundary layer on the vehicle as shown in Fig. 9. Here, y is the radial coordinate with y_w denoting the wall location, and the data corresponds to $s/D \simeq 1.3$ and is representative of other locations on the afterbody. In the near-wall region, where DES works in the RANS mode, eddy viscosity levels are found to be comparable or smaller than the molecular viscosity. This implies that the boundary layer on the conical frustum is close to being laminar. In such a situation, the temperature gradient at the wall is mainly determined by the conditions at the boundary layer edge, i.e. by the core flow, which depends on the LES part of the simulation. The RANS model which is effective only in the near wall boundary layer has minimal effect on the heat transfer rate to the vehicle. As pointed out earlier, the core flow temperature in the fine grid solution is significantly lower than that computed on the baseline and coarse grids. Hence the lower heating rate prediction on the fine grid.

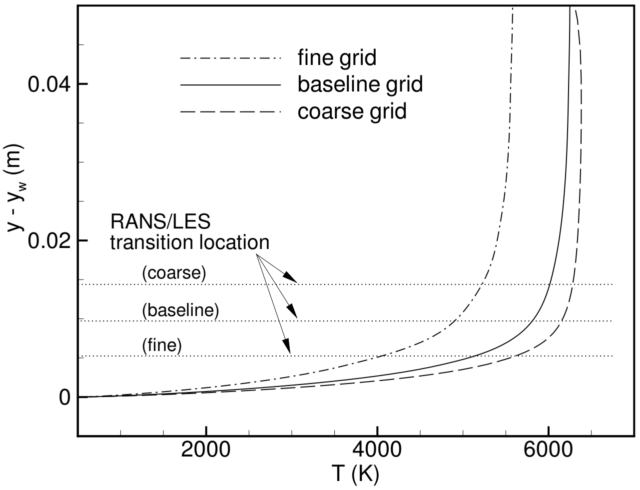

Figure 9. Temperature profile across the recirculation bubble on the Fire II afterbody as obtained using the fine, baseline, and coarse grids. The data corresponds to $s/D \simeq 1.3$ station.

Conclusions

The present work employs detached eddy simulation to study the hypersonic base flow for a capsule re-entry configuration. Multi-block finite-volume grids are generated to resolve the strong shocks and expansions typical of hypersonic blunt body flows, and to meet the requirements of detached eddy simulation in the wake. Time-averaging yields almost uniform pressure along the frustum and higher value in the base stagnation region. The afterbody heat transfer rate of these low Re flows is mostly determined by the LES part of the simulation, and not by the RANS model effective in the near-wall region. It is also found to be relatively insensitive to variations in the RANS/LES transition location. Grid refinement in the DES focus region results in lower eddy viscosity which in turn leads to a larger recirculation zone, higher pressure and lower heating rate on the afterbody. The fine grid results are found to be close to the fine-grid laminar solution, with vanishing eddy viscosity. Thus, unlike fully turbulent flows, DES of this low Re hypersonic configuration approaches direct simulation of the flow. Control of the numerical dissipation is therefore essential to obtain a grid-converged solution. On the whole, the current work is a careful application of DES to a low Reynolds number and high Mach number re-entry configuration. It gives valuable insights into the numerical and modeling issues involved in the DES methodology.

Acknowledgments

This work was supported by Air Force Office of Scientific Research (AFOSR) under Grant No. FA9550-04-1-0341. The views and conclusions contained herein are those of the authors and should not be interpreted as necessarily representing the official policies or endorsements, either expressed or implied, of the AFOSR or the U.S. Government. The first author would also like to thank the Department of Aerospace Engineering, Indian Institute of Technology Madras, India, for its support during compilation of the results.

References

[1] Wright, M.J., Brown, J.L., Sinha, K., Candler, G.V., Milos, F.S., Prabhu, D.K., "Validation of Afterbody Aeroheating Predictions for Planetary Probes: Status and Future Work," *2nd International Planetary Probe Workshop*, August 2004.

[2] Brown, J.L., "Turbulence Model Validation for Hypersonic Flows," AIAA Paper 2002-3308, June 2002.

[3] Nance, R.P., Hollis, B.R., Horvath, T.J., Alter, S.J., and Hassan, H.A., "Computational Study of Hypersonic Transitional Wake Flow," *Journal of Thermophysics and Heat Transfer*, Vol. 13, No. 2, 1999.

[4] Shur, M., Spalart, P.R., Strelets, M., and Travin, A., "Detached Eddy Simulation of an Airfoil at High Angle of Attack," *4th International Symposium on Engineering Turbulence Modeling and Measurements*, Corsica, 1999.

[5] Forsythe, J.R., Hoffman, K.A., and Squires, K.D., "Detached-Eddy Simulation with Compressibility Corrections Applied to a Supersonic Axisymmetric Base Flow," AIAA Paper 2002-0586, Jan 2002.

[6] Sinha, K., Barnhardt, M., and Candler, G.V., "Detached Eddy Simulation of Hypersonic Base Flows with Application to Fire II Experiments," AIAA Paper 2004-2633, June 2004.

[7] Sloucomb, T.H., "Project Fire II Afterbody Temperatures and Pressures at 11.35 Kilometers per Second," NASA TM X-1319, 1996.

[8] Lees, L., "Hypersonic Wakes and Trails," *AIAA Journal*, Vol. 2, No. 3, 1964.

[9] MacCormack, R. W., and Candler, G. V., "The Solution of the Navier-Stokes Equations Using Gauss-Seidel Line Relaxation," *Computers and Fluids,* Vol. 17, No. 1, 1989, pp. 135-150.

[10] Sinha, K., and Candler, G.V., "An Accurate Implicit Formulation of a Two-Equation Turbulence Model," AIAA Paper 98-2649, June 1998.

[11] Wright, M. J., Sinha, K., Olejniczak, J., Candler, G. V., Magruder, T.D. and Smits, A.J., "Numerical and Experimental Investigation of Double-cone Shock Interactions," *AIAA Journal*, Vo. 38, No. 12, 2000, pp. 2268-2276.

[12] Spalart, P.R., and Allmaras, S.R., "A One-Equation Turbulence Model for Aerodynamic Flows," AIAA Paper 92-0439, Jan. 1992.

[13] Wright, M. J., Candler, G. V., and Prampolini, M., "Data-Parallel Lower-Upper Relaxation Method for the Navier-Stokes Equations," *AIAA Journal,* Vol. 34, No. 7, 1996, pp. 1371-1377.

[14] Sinha, K., "Reynolds-averaged Navier-Stokes Simulation of Fire II Re-entry Configuration," *Proceedings of the 25th International Symposium on Shock Waves*, Bangalore, India, July 2005.

[15] Spalart, P.R., "Young-Person's Guide to Detached-Eddy Simulation Grids," NASA CR 2001-211032, July 2001.

[16] Sinha, K., "Effect of Reynolds Number on Detached Eddy Simulation of Hypersonic Base Flow," AIAA Paper 2007-1457, Jan. 2007.